Airy structure in $^{16}O+^{16}O$ elastic scattering between 5 and 10 MeV/nucleon

F. Michel,[1] G. Reidemeister,[2] and S. Ohkubo[3]
[1]*Faculté des Sciences, Université de Mons-Hainaut, B-7000 Mons, Belgium*
[2]*Faculté des Sciences, Université Libre de Bruxelles, CP229, B-1050 Bruxelles, Belgium*
[3]*Department of Applied Science and Environment, Kochi Women's University, Kochi 780-8515, Japan*

(Received 7 November 2000; published 22 February 2001)

We have applied the barrier-wave/internal-wave decomposition technique to $^{16}O+^{16}O$ elastic scattering optical model angular distributions between 75 and 145 MeV, an energy region where strong refractive effects—in particular Airy maxima and minima—are clearly observed; this technique, introduced in a semiclassical framework more than 20 years ago by Brink and Takigawa, and which was successful in clarifying the light-ion elastic scattering mechanism, has practically never been used in the context of light heavy-ion scattering. The decomposition is accomplished by using a fully quantum-mechanical method, which bypasses the intricacies of the semiclassical approach. The Airy minima are found to be due to the interference of the barrier-wave and internal-wave subamplitudes; the presence of a substantial internal-wave contribution demonstrates in a very clear way the exceptional transparency displayed by the $^{16}O+^{16}O$ system. The results obtained contrast with those of the nearside/farside decomposition technique, where the Airy minima are fully carried by the farside contribution. By combining the two approaches it is possible to calculate in a straightforward way the two components underlying the structure of the farside component, which up to now have been obtained through delicate semiclassical calculations or the use of an approximate empirical method. The complicated evolution of the full elastic cross section can eventually be explained in terms of the interference of several subamplitudes with a much smoother, and thus much simpler to understand, behavior. A barrier-wave/internal-wave decomposition of the 132 MeV $^{16}O+^{12}C$ and 100 MeV $^{18}O+^{12}C$ elastic scattering amplitudes is also presented.

DOI: 10.1103/PhysRevC.63.034620 PACS number(s): 24.10.Ht, 25.70.Bc

I. INTRODUCTION

The systematic measurement and phenomenological analysis, for a few selected systems, of elastic scattering angular distributions on a broad range of energies and angles, has recently resulted in a considerable progress in the understanding of the dynamics of light heavy-ion scattering [1]. Comprehensive data sets are indeed now available for the $^{12}C+^{12}C$ [2], $^{16}O+^{12}C$ [3–5], and $^{16}O+^{16}O$ [6,7] systems up to 10 MeV per nucleon (and beyond), and optical model potentials varying reasonably smoothly with energy and reproducing the complicated energy dependence of the data have been extracted [4–8].

In the meantime, a series of seminal papers [9–12,1,13] were devoted to the interpretation of the optical model results in more intuitive terms. Most of these studies were carried out within the frame of the so-called nearside/farside (N/F) decomposition method introduced by Fuller [14] some 25 years ago, where the scattering amplitude, $f(\theta)$, is split into two contributions, $f_N(\theta)$ and $f_F(\theta)$, corresponding to classical trajectories with positive and negative deflection angles, respectively. These analyses revealed that the broad structures observed in the experimental angular distributions and excitation functions for these systems are due to refractive effects, which in an optics language were described in terms of the Airy maxima and minima of rainbow wave theory [15].

In the N/F approach, the Airy structure does however not result from an interference between the nearside and farside components, but is fully carried by the farside contribution to the scattering amplitude [1]. The N/F decomposition thus does not supply a direct explanation of the Airy structure observed in some light heavy-ion systems: to understand this structure, one has to invoke the existence, in the farside component itself, of two interfering contributions corresponding to negative deflection angle trajectories with different angular momenta [10] (usually noted $l_<$ and $l_>$). This interpretation is substantiated, in a ray optics analogy, by resorting to the concept of deflection function [15] (which strictly speaking is only applicable in the absence of absorption), or more generally by invoking semiclassical approaches like that of Knoll and Schaeffer [16], which in a complex trajectory interpretation associate semiclassical subamplitudes to each turning point found in the complex r plane. Since the contribution with the lowest angular momentum $l_<$ only survives within an incomplete absorption context—indeed, increasing the imaginary part of the optical potential in the central region makes the Airy oscillations disappear [17]—the observation of Airy oscillations bears testimony to the transparency of the interaction in the investigated system.

Optical model analyses have revealed that a consistent description of the evolution of the Airy oscillations with energy and angle, seen in the elastic angular distributions for transparent systems, can only be reached if refraction is strong enough—in other words if the real part of the optical potential is sufficiently deep [1]. As a matter of fact, the depths of the potentials compatible with experiment are found to be in good agreement with those predicted by folding model calculations using a convenient nucleon-nucleon effective interaction [1,18]. It is the considerable depth of the potential that makes possible the appearance of supernumerary bows at angles smaller than that of the main rainbow and produces the observed Airy structure. Again using an optics language, the index of refraction n found necessary to reproduce the bending of the nuclear trajectories, which is linked to the potential depth V by the simple equation

$$n(r)=\sqrt{1-\frac{V(r)}{E_{\mathrm{c.m.}}}}, \tag{1}$$

greatly exceeds that of water at small distances: indeed at incident energies of about 5 MeV per nucleon, it even exceeds that of diamond ($n>2.5$).

Although the N/F decomposition of Fuller has taken the lion's share in most of the studies referred to above, it is not the only method available to decompose the scattering amplitude into semiclassical components with an intuitively appealing interpretation. Indeed, not long after Fuller's work, Brink and Takigawa [19] introduced another scheme, known as the barrier-wave/internal-wave (B/I) decomposition, which makes sense provided the real part of the potential is deep enough for the effective potentials active in the scattering to display ''potential pockets.'' In this method, the elastic scattering amplitude $f(\theta)$ is split into two contributions, $f_B(\theta)$ and $f_I(\theta)$, corresponding, respectively, to that part of the incident flux which is reflected at the barrier of the effective potential, and that which penetrates the nuclear interior and reemerges in the entrance channel after reflection from the most internal turning point. This approach provided considerable help in elucidating the mechanism of the ALAS phenomenon observed in elastic scattering for some light-ion systems [19–21], and it supplied for the first time unquestionable evidence for a substantial transparency in the scattering of composite projectiles like the α particle [22,23].

It is the purpose of the present paper to show that the decomposition method of Brink and Takigawa complements nicely the N/F method of Fuller, and that in a context of incomplete absorption it provides an illuminating interpretation of the occurrence of the Airy structure seen in light heavy-ion scattering angular distributions. To this end, we will investigate in a systematic way the properties of the ^{16}O$+^{16}$O optical model potential at incident energies between about 5 and 10 MeV per nucleon (this last energy is that where the potential loses its ''pocket'' at the grazing angular momentum). Although the B/I decomposition for complex potentials was initially introduced within a semiclassical framework [19]—thus requiring the localization of complex turning points and the evaluation of action integrals in the complex plane, which makes it rather difficult to implement and restricts its use to analytical potentials—it is possible to obtain the same information within a full quantum-mechanical frame [24], using any conventional optical model code, by taking advantage of the response of the elastic scattering amplitude to small modifications of the optical potential inside of the barrier radius; this much simpler method—which we will refer to as the quantum-mechanical perturbative method—will be used consistently here.

The organization of this paper is as follows. In Sec. II, after introducing the ^{16}O$+^{16}$O potentials which are used in our calculations, we briefly recall the salient features of the N/F and B/I decomposition techniques, and we give an exhaustive presentation of the results of our calculations between 75 and 145 MeV incident energies. Section III is devoted to a rapid presentation of preliminary results for other systems, while Sec. IV contains our conclusions. A preliminary account of this work has recently been presented in Ref. [25].

II. ANALYSIS OF ^{16}O+^{16}O ELASTIC SCATTERING FOR INCIDENT ENERGIES BETWEEN 75 AND 145 MeV

A. The ^{16}O+^{16}O optical model potentials

In a recent publication, Nicoli *et al.* [6] present an optical model analysis of their Strasbourg Vivitron ^{16}O$+^{16}$O data at nine incident energies ranging from 75 to 124 MeV. The potentials used are either purely phenomenological [their real part has a Woods-Saxon squared (WS2) geometry, while their imaginary part is the sum of a WS2 volume term and a surface term with a Woods-Saxon derivative (WSD) shape], or ''microscopic'' (real part supplied by the folding model, imaginary part sum of WS2 and WSD components). The phenomenological potentials thus read

$$\begin{aligned}U(r)=V(r)+iW(r)=V_C(r)-U_0 f(r;R_R,a_R)\\ -i[W_0 f(r;R_I,a_I)+W_D g(r;R_D,a_D)],\end{aligned} \tag{2}$$

where

$$f(r;R,a)=\frac{1}{\{1+\exp[(r-R)/2a]\}^2}, \tag{3}$$

$$g(r;R,a)=\frac{4\exp[(r-R)/a]}{\{1+\exp[(r-R)/a]\}^2}. \tag{4}$$

Note that in the expression of the WS2 form factor we have multiplied the diffuseness a by a factor of 2, which has the advantage of preserving the original meaning of the diffuseness a: indeed with this convention $f(r;R,a)$ behaves asymptotically, like for a more traditional WS form factor, as $\exp[-(r-R)/a]$.

The analysis of Ref. [6] is an outgrowth of an earlier optical model analysis presented in Nicoli's thesis [26], where the imaginary part of the potentials did not include a surface component. Whereas the agreement with the data is of course better with the heavier parametrization, the simpler potentials of Ref. [26] already provide a very satisfactory description of the main trends of the complicated energy and angular dependence of the data. The better agreement obtained in Ref. [6] turns out to result at some energies from the use of very small imaginary diffusenesses, either in the surface term at large distances or in the volume term at smaller radii; we will see below that these energy-dependent features introduce complications in the scattering dynamics and make its energy dependence more irregular. As we intend to concentrate here on a global explanation of the angular and energy dependence of the data, we decided to stick in the following to Nicoli's thesis potential parameters.

In another very recent paper, Khoa *et al.* [7] present a detailed optical model analysis of HMI and GANIL ^{16}O

TABLE I. Optical model parameters of Nicoli [26] between 75 and 124 MeV, and of Khoa *et al.* [7] at 145 MeV, used in the present work, together with the volume integrals per nucleon pair j_V and j_W of the real and imaginary parts of these potentials (energies in MeV, lengths in fm, volume integrals in MeV fm^3).

E_{lab}	U_0	R_R	a_R	W_0	R_I	a_I	W_D	R_D	a_D	j_V	j_W
75.0	412	3.97	0.746	67.9	2.26	1.130				331.7	27.5
80.6	412.6	3.97	0.770	51.0	2.69	1.320				336.9	33.8
87.2	414.8	3.97	0.780	31.14	4.528	1.175				340.8	45.4
92.4	420.7	3.97	0.825	11.53	7.237	0.257				355.7	57.8
94.8	419	3.97	0.778	12.24	7.02	0.349				343.7	54.7
98.6	414	3.97	0.779	15.44	6.598	0.566				340.0	52.7
103.1	409.6	3.97	0.780	15.68	6.80	0.623				336.5	58.1
115.9	412	3.97	0.752	14.77	6.849	0.425				332.8	59.0
124	420	3.97	0.789	15.13	7.105	0.452				346.9	65.6
145	385.3	4.18	0.715	9.107	6.800	0.433	16.01	5.421	0.435	349.6	76.5

$+^{16}O$ data at energies ranging from 250 to 1120 MeV [27–29]; JAERI data at 124 MeV and at 145 MeV [30,31] are also included in their systematics. As in Ref. [6], phenomenological and folding potentials are used together with imaginary potentials with WS2 + WSD geometry.

As the present study is restricted to incident energies lower than 150 MeV, the potential of Khoa *et al.* at 145 MeV will be the only one used in the forthcoming. It is however important to point out that the real parts of the potentials they obtain at higher energies are smoothly connected to those at 124 and 145 MeV, and to those of the potentials obtained by Nicoli down to 75 MeV. Indeed the volume integrals per nucleon pair j_V of the phenomenological potentials of Nicoli and of Khoa *et al.* decrease smoothly from about 340 MeV fm^3 at low energy to 210 MeV fm^3 at 1120 MeV; these potentials thus appear to belong to a single potential family. This family coincides with that selected ten years ago, on the basis of dispersion relation arguments, by Kondo *et al.* [32] from three phase-equivalent potential families giving comparable fits to (limited angular range) 350 MeV $^{16}O+^{16}O$ elastic scattering data. Subsequent analyses involving more extensive data sets [33,34,30,31,29] proved that this choice was indeed the correct one. The selection of a unique potential family makes possible the identification of the orders of the various Airy minima seen in experiment, A_1 being by definition the last minimum showing up when energy increases (at 90°, the latter appears at about 200 MeV incident energy for the present system).

The parameters of the potentials that will be used in the rest of this paper are collected in Table I, together with their real and imaginary volume integrals per nucleon pair j_V and j_W; a comparison of their predictions with the experimental data appears in Fig. 1. Instead of plotting the cross sections $\sigma(\theta)$ as their ratio to the Mott scattering cross section $\sigma_M(\theta)$, as is done most of the time, we have plotted them as their ratio to $[\sigma_R(\theta)+\sigma_R(\pi-\theta)]$, where σ_R is the Rutherford cross section; this convention will be used consistently throughout the present paper each time we have to display symmetrized cross sections. The main reason for departing from common practice is that at the energies considered here, the Mott cross section displays considerable structure around 90°; plotting the cross sections as their ratio to Mott scattering thus introduces artificial oscillations, which unnecessarily complicate the (already fairly complex) scattering pattern and tend to hide the interesting physical features. Plotting $\sigma(\theta)/[\sigma_R(\theta)+\sigma_R(\pi-\theta)]$ does not present this shortcoming, while eliminating the divergence of the cross sections

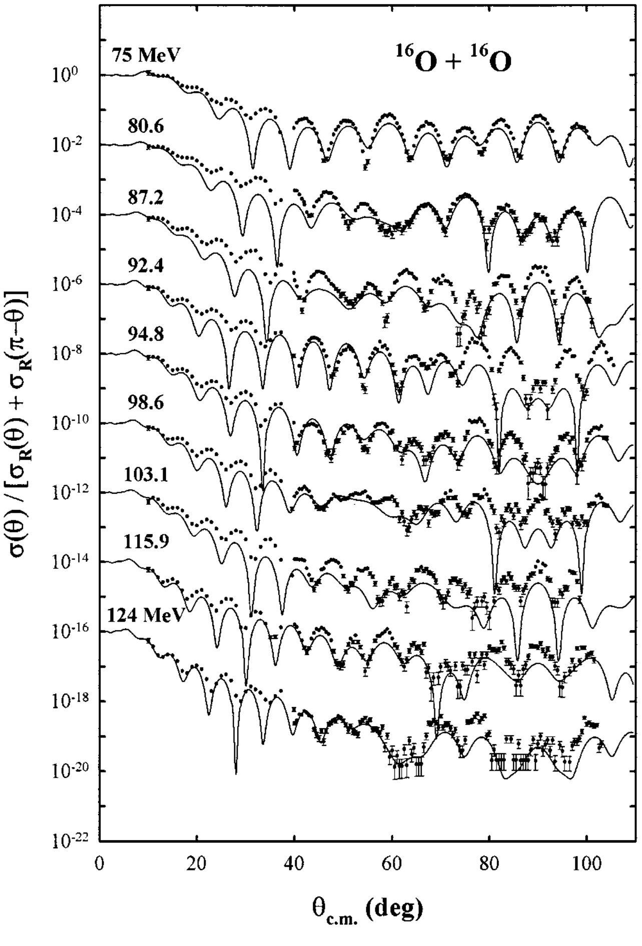

FIG. 1. Comparison of the optical model calculations of Nicoli [26] with the experimental $^{16}O+^{16}O$ elastic scattering angular distributions between 75 and 124 MeV [26,6].

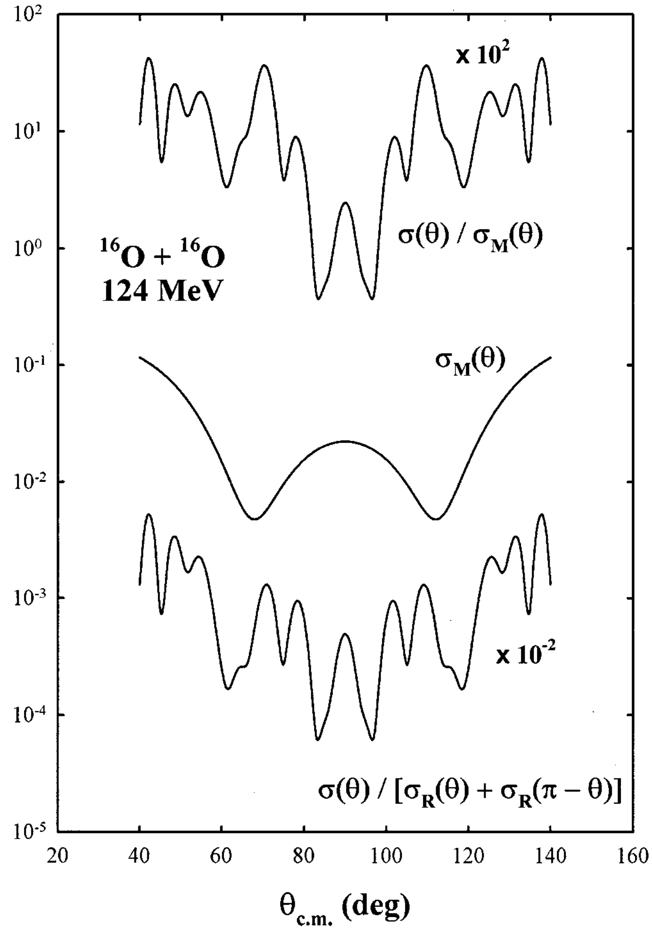

FIG. 2. Plot of the ratio of the 124 MeV ^{16}O+^{16}O optical model cross section $\sigma(\theta)$ to the Mott cross section σ_M (top) and to the symmetrized Rutherford cross section $\sigma_R(\theta)+\sigma_R(\pi-\theta)$ (bottom), and of the pure Mott angular distribution at this energy (center).

around 0 and 180° and preserving the fore-aft symmetry of the cross sections. Plots of the 124 MeV optical model angular distribution using the two conventions, and of pure Mott scattering at this energy, is presented in Fig. 2; one sees that the artificial enhancement of the cross section around 65° (and 115°) and the depression around 90° of the σ/σ_M plot have disappeared, while the Airy minima around 60° (and 120°) stand out much more conspicuously in this less conventional representation.

In Fig. 3, we display the effective potential curves corresponding to Nicoli's potential at 124 MeV for angular momenta ranging from 20 to 40. One sees that the potential is deep enough for potentials pockets—an important ingredient in the forthcoming B/I decomposition analysis—to survive up to $l=30$; the critical center of mass energy corresponding to this disappearance is about 70 MeV. Khoa *et al.* [7] potential at 124 MeV displays very similar properties.

B. The nearside/farside decomposition

We summarize here the main ingredients of the N/F decomposition method of Fuller [14], and the results obtained in Refs. [26,6,7] for the ^{16}O+^{16}O system.

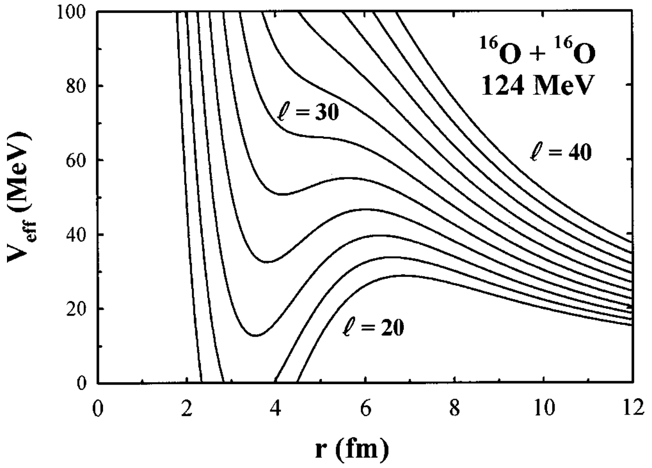

FIG. 3. Effective potential curves for angular momenta l between 20 and 40, calculated with the real part of the ^{16}O+^{16}O 124 MeV optical potential of Nicoli [26].

The method of Fuller makes possible the decomposition of the scattering amplitude $f(\theta)$ into subamplitudes $f_N(\theta)$ and $f_F(\theta)$, corresponding, respectively, to trajectories with positive and negative deflection angles (Fig. 4). In fact, this clever technique circumvents the stationary phase evaluation of the integrals corresponding to these paths, which are encountered when one substitutes the large l asymptotic formulas for the Legendre polynomials in the partial wave expansion of $f(\theta)$ and one replaces the sum over the partial waves by an integral by resorting to the Poisson summation formula [21]: indeed the decomposition is achieved in a more direct way by replacing the Legendre polynomials $P_l(\cos\theta)$ in the partial wave series by their "travelling wave" components $\tilde{Q}_l^{(-)}$ and $\tilde{Q}_l^{(+)}$, which are defined by the following combinations of Legendre polynomials P_l and of Legendre functions of the second kind Q_l:

$$\tilde{Q}_l^{(\pm)}=\frac{1}{2}\left[P_l(\cos\theta)\mp i\frac{2}{\pi}Q_l(\cos\theta)\right]. \tag{5}$$

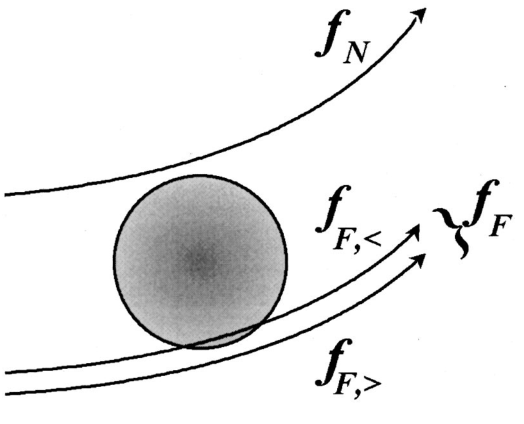

FIG. 4. Schematic representation of the classical trajectories contributing to the nearside (f_N) and farside (f_F) components of the elastic scattering amplitude; the latter contains generally contributions from deeply penetrating ($f_{F,<}$) and more peripheral ($f_{F,>}$) trajectories.

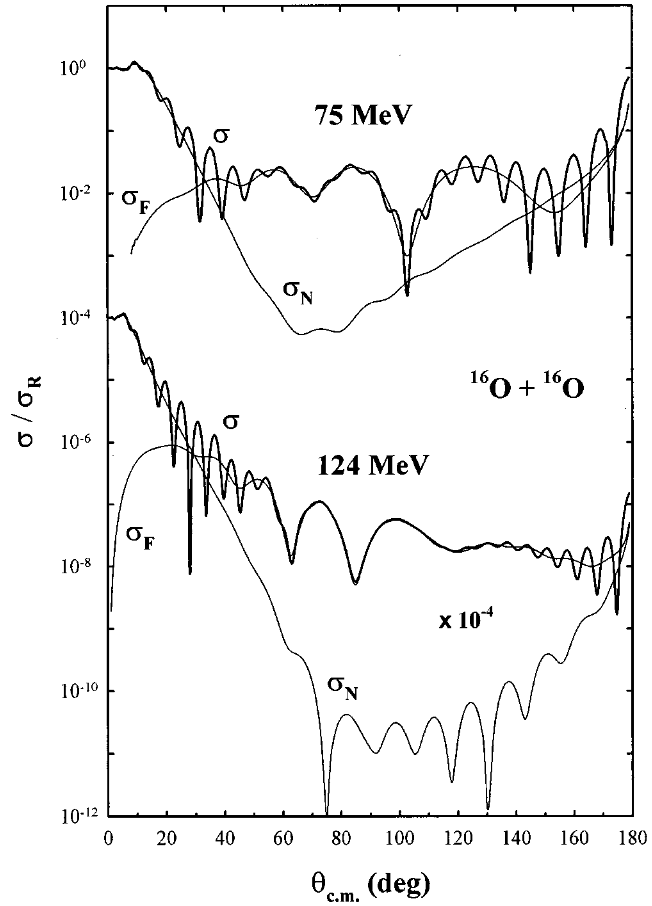

FIG. 5. Nearside/farside decomposition of the ^{16}O+^{16}O optical model angular distributions at 75 MeV and 124 MeV incident energies.

The Rutherford scattering amplitude has likewise to be decomposed into its nearside and farside components $f_{R,N}(\theta)$ and $f_{R,F}(\theta)$, which can be obtained in closed form [14].

The two components of the ^{16}O+^{16}O scattering amplitude $f(\theta)$ obtained using this technique display features already encountered for this and other systems at higher energies [5,7]. At small angles, the cross section $\sigma(\theta)$ is dominated by the nearside amplitude $f_N(\theta)$, and the interference between the nearside and farside components of f accounts for the Fraunhofer oscillations observed below about 50°, as is seen in Fig. 5, which displays the results of the N/F decomposition at 75 and 124 MeV, and where for clarity the cross sections have not been symmetrized and are plotted as their ratio to Rutherford scattering. At larger angles the cross section is dominated by the farside contribution; at low energy however, the influence of the nearside component persists on the whole angular range, and interference effects between the two subamplitudes give rise in the full cross section to oscillations persisting on most of the angular range.

This persistence of the influence of the nearside component on the whole angular range at 75 MeV is interpreted in Ref. [6] as being due to the fact that the farside contribution extends beyond 180° at low energy (which implies that the rainbow angle is larger than 180°—one can thus speak of ‘‘glory scattering’’ at these energies), but that deflection angles exceeding 180° are associated in the N/F decomposition to the nearside component f_N. Whereas the interference oscillations between f_N and f_F have a diffractive origin at small angles, those observed at larger angles are thus in this interpretation caused by refraction. We will see in Sec. II D how this interpretation is confirmed by the B/I decomposition. Anyhow it is difficult to discern these interference oscillations at midangles in the data, since much stronger oscillations are induced there by symmetrization effects (see Fig. 1).

At very large angles ‘‘backangle Fraunhofer oscillations’’ [17] are always present since the nearside and farside amplitudes become equal at 180°; however this is of no practical relevance for symmetric systems, since in that case this feature is completely hidden by the Coulomb divergence.

The gross structure observed in the unsymmetrized cross sections in the midangle region is seen to be carried by the farside component of the scattering amplitude. Whereas the N/F decomposition as such thus does not clarify the origin of these oscillations, a deflection function interpretation suggests, as explained in the Introduction, that for angles smaller than the rainbow angle there are two trajectories leading to the same negative deflection angle; interference between these trajectories, which carry different phases, is responsible for the broad oscillations seen in the farside contribution. This interference mechanism is identical to that proposed by Airy to give a wave contents to the Descartes ray picture of the rainbow, in order to account for the occurrence of supernumerary bows on the lit side of the primary rainbow [35–37]; the minima seen in σ_F have therefore become known as Airy minima [1].

The decomposition of the farside amplitude f_F into two components with different angular momenta (which to conform to general usage will be noted $f_{F,<}$ and $f_{F,>}$) can in principle be carried out by resorting to semiclassical approaches like that of Knoll and Schaeffer [16]; however this technique, which is complicated to use in numerical calculations (in particular the topology of the turning points trajectories changes in a complicated way with the optical model parameters [38,39]), has rarely been used in this context, and then only at relatively high incident energy (^{12}C+^{12}C at 159 and 240 MeV [39], ^{13}C+^{12}C at 260 MeV [38], ^{16}O+^{12}C at 608 MeV [39], and ^{16}O+^{16}O at 350 MeV [27]). A simpler approximate method, due to da Silveira and Leclercq-Willain [40] (sometimes referred to as the ‘‘interpolated-envelope technique’’ [17,41]) has also been used to decompose qualitatively the farside amplitude into its two components; it is based on the fact that the cross section $\sigma(\theta)$ corresponding to the sum of the two subamplitudes $f_{F,<}(\theta)$ and $f_{F,>}(\theta)$ oscillates between the two limits $E_+(\theta)=[\sigma_{F,<}(\theta)^{1/2}+\sigma_{F,>}(\theta)^{1/2}]^2$ and $E_-(\theta)=[\sigma_{F,<}(\theta)^{1/2}-\sigma_{F,>}(\theta)^{1/2}]^2$, which define envelopes which can easily be drawn when the oscillations in $\sigma(\theta)$ are well defined. Comments on the application of this method to the data investigated here will be made in the next section.

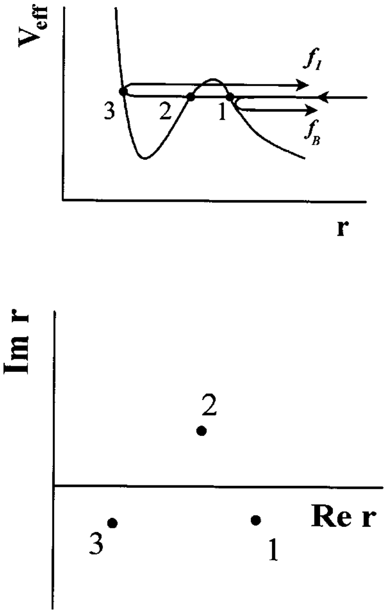

FIG. 6. Schematic representations of the classical trajectories contributing to the barrier-wave (f_B) and internal-wave (f_I) components of the elastic scattering amplitude (top), and of the location of the three turning points in the complex plane (bottom).

C. The barrier-wave/internal-wave decomposition

1. Semiclassical approach

Before we present the results of the barrier-wave/internal-wave decomposition of the scattering amplitude to the ^{16}O $+^{16}$O system, we recall the main ingredients of this technique, first presented within a WKB context by Brink and Takigawa [19,21].

When the real part $V(r)$ of the optical potential is deep enough for the effective potential

$$V_{eff}(r)=V(r)+\frac{\hbar^2}{2\mu}\frac{l(l+1)}{r^2} \qquad (6)$$

to display a pocket, three turning points generally play an important role in a semiclassical description of the scattering. These turning points, which are by definition the zeros of $E_{\mathrm{c.m.}}-V_{eff}(r)-iW(r)$, are real if the incident energy is less than that of the top of the barrier V_B and if $W=0$, but they move away from the real axis when $E_{\mathrm{c.m.}}>V_B$ and/or $W\neq 0$ (Fig. 6). The main ingredients in a WKB approach are the action integrals

$$S_{ij}=\int_{r_i}^{r_j} dr\left\{\frac{2\mu}{\hbar^2}[E_{\mathrm{c.m.}}-V_{eff}(r)-iW(r)]\right\}^{1/2}, \qquad (7)$$

which have to be evaluated in the complex plane between the turning points r_i and r_j of the problem (here and in the following the angular momentum index l will be dropped if not needed). In a three turning points problem, the action integrals to evaluate are $S_1\equiv S_{1\infty}$, S_{21}, and S_{32}. The first one is nothing but the action integral appearing in the one turning point WKB approach [15], while S_{21} is related to the barrier penetrability. Brink and Takigawa [19] have shown that, if the imaginary part of S_{32} is large—which happens in most cases of practical interest when absorption is not too weak—multiple reflections inside the potential pocket can be neglected, and the elastic S matrix can be decomposed into two contributions

$$S\simeq\frac{e^{2iS_1}}{N}+\frac{e^{2i(S_{32}+S_{21}+S_1)}}{N^2} \qquad (8)$$

$$\equiv S_B+S_I, \qquad (9)$$

where N, which is often close to unity, is a function of S_{21} and is related to the barrier penetrability; these contributions correspond to the part of the incident flux which is reflected at the barrier (S_B), and to that which crosses the barrier and reemerges after reflection at the most internal turning point (S_I), respectively. From these components of the S matrix one can derive the barrier-wave and internal-wave scattering amplitudes $f_B(\theta)$ and $f_I(\theta)$, which are defined in conventional notations as

$$f_B(\theta)=f_R(\theta)+\frac{1}{2ik}\sum_l (2l+1)e^{2i\sigma_l}[S_B(l)-1]P_l(\cos\theta), \qquad (10)$$

$$f_I(\theta)=\frac{1}{2ik}\sum_l (2l+1)e^{2i\sigma_l}S_I(l)P_l(\cos\theta). \qquad (11)$$

In practice, the accuracy of the semiclassical decomposition can be checked by comparing the full semiclassical scattering cross section $|f_B(\theta)+f_I(\theta)|^2$ with that supplied by the optical model calculations. One has to keep in mind that in some cases the problem may be dominated by more than three active turning points; this happens, e.g., when the real and imaginary parts of the potential have different geometries and the diffuseness of the imaginary potential is very small (say, less than about 0.2 fm): one then observes reflection at this sharp boundary, to which corresponds an additional turning point. A general approach to the multiturning point problem based on a wave propagation matrix method has been proposed by Lee and Takigawa [42].

2. Quantum-mechanical calculation of the barrier and internal contributions

Because the semiclassical method of Brink and Takigawa [19] requires the localization of complex turning points and the evaluation of action integrals along complex paths, its practical implementation is not too easy and, as a matter of fact, it has been used infrequently as such in the literature. However, a much more straightforward technique [24], based on simple modifications of any optical model computer code, makes possible the separation of the scattering amplitude into its barrier and internal wave components, provided the effective potential displays a pocket for all the active partial waves. The basic idea of this technique is to study the response of the S matrix to perturbations of the optical potential; to first order the action integrals behave linearly in the perturbation $g(r)$, and if the latter is of short range, S_{32} is the only action integral affected by the modification of the potential. Taking Eq. (8) into account, a simple derivation then shows that three successive optical model calculations, using the original potential $U(r)$ and the modified potentials $U(r) \pm g(r)$ (to which correspond S matrix elements which will be noted $S^{(0)}$ and $S^{(\pm)}$, respectively), make possible the calculation of S_B and S_I; indeed one obtains [24]

$$S_I = -\frac{\Delta^+ \Delta^-}{\Delta^+ + \Delta^-}, \tag{12}$$

$$S_B = S^{(0)} - S_I, \tag{13}$$

where $\Delta^{\pm} \equiv S^{(\pm)} - S^{(0)}$.

In contrast with the semiclassical approach, the sum of the barrier and internal components of the S matrix or of the scattering amplitude supplied by this method coincide by construction with the exact result. The perturbation used can be complex; in the following we will restrict to imaginary perturbations, that is, we will increase/decrease the imaginary part of the optical potential at small distances. In practice, the perturbation has to be chosen so that only the most inside turning point is affected; this requires a rather rapid decrease of its form factor, but this decrease must be smooth enough so that no extra reflection appears in the potential pocket—in other words no additional spurious turning point should be introduced in the calculation; here a perturbation of the type suggested in Ref. [24] will be used, that is

$$g(r) = i W_1 \mathrm{e}^{-(r/\rho)^4}. \tag{14}$$

In practice, as recommended in Ref. [24], W_1 can assume values equal to about one tenth of the strength of the imaginary potential strength, while ρ should be about half the barrier radius at the grazing angular momentum.

The barrier and internal wave S matrices and amplitudes supplied by the method can be considered as reliable only if they do not depend critically on the parameters of the perturbation; of course, when one of the two components is much smaller than the other, the estimates supplied by the method, which is based on the calculation of small differences in the optical model S matrix, inevitably carry some errors; as will shown below, these show up as fluctuations when the perturbation parameters are changed. We finally note that a refinement of the method, consisting in the introduction of a stronger extra imaginary potential with a strength W_2 and the same form factor as the perturbation $g(r)$, as proposed in Ref. [24], has been used to improve the barrier S matrix at low angular momenta (see below).

D. Barrier-wave/internal-wave decomposition: The ^{16}O+^{16}O system

1. Selected energies

In this subsection, we present the result of the B/I decomposition of the ^{16}O+^{16}O optical model scattering amplitude at 75 and 124 MeV; a general discussion of the energy evolution of the two components from 75 to 145 MeV will be presented in Sec. II D 2.

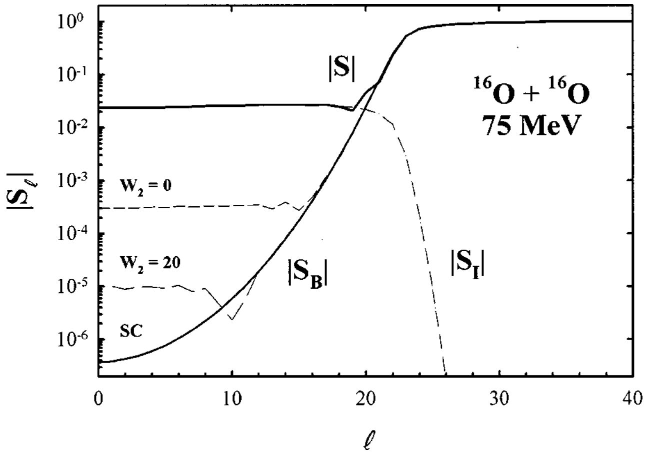

FIG. 7. Decomposition of the ^{16}O+^{16}O optical model S matrix into its barrier-wave and internal-wave components at 75 MeV, using the quantum-mechanical perturbative approach of Ref. [24], without ($W_2 = 0$) and with ($W_2 = 20$) an additional absorptive potential; the curve labeled SC is the barrier contribution obtained from a semiclassical calculation.

The basic quantities supplied by the B/I decomposition are the barrier-wave and internal-wave S matrix elements S_B and S_I. Their moduli at 75 MeV are plotted as a function of the angular momentum l in Fig. 7, together with the modulus of the full optical model S matrix (the so-called ‘‘absorption profile’’ [1]) . Calculations were carried out using the values $W_1 = 2.5$ MeV and $\rho = 3.25$ fm for the parameters of the perturbation in Eq. (14). As is usual for systems displaying incomplete absorption [1], one sees that the full S matrix shows two distinct behaviors according to the value of l: whereas at large l, the S matrix behaves like that provided by strong absorption models, at small $l (l < 20)$ one observes a saturation to a value of about 2×10^{-2}. The B/I decomposition shows that the barrier contribution to the S matrix tends to very small values at small l, and that the saturation observed below $l = 20$ is entirely due to the internal wave contribution; the interference between the two contributions is responsible for the oscillations seen near $l = 20$ in the total S matrix.

It is interesting from a technical point of view to comment on the effect of introducing an extra absorption in the quantum-mechanical calculation of the barrier and internal contributions [24] to improve the barrier S matrix, as mentioned at the end of the previous subsection. In Fig. 7, we show the results of calculations carried out without and with such an extra absorption (in the latter case with a strength $W_2 = 20$ MeV), as well as the result of a full semiclassical calculation. Whereas the internal part of the S matrix is the same in the three calculations at the scale of the figure, the barrier part supplied by the quantum-mechanical calculation at low l with $W_2 = 0$ is larger than the semiclassical one by about three orders of magnitude; using $W_2 = 20$ MeV improves the results by more than one order of magnitude. The residual disagreement has hardly any consequence on the

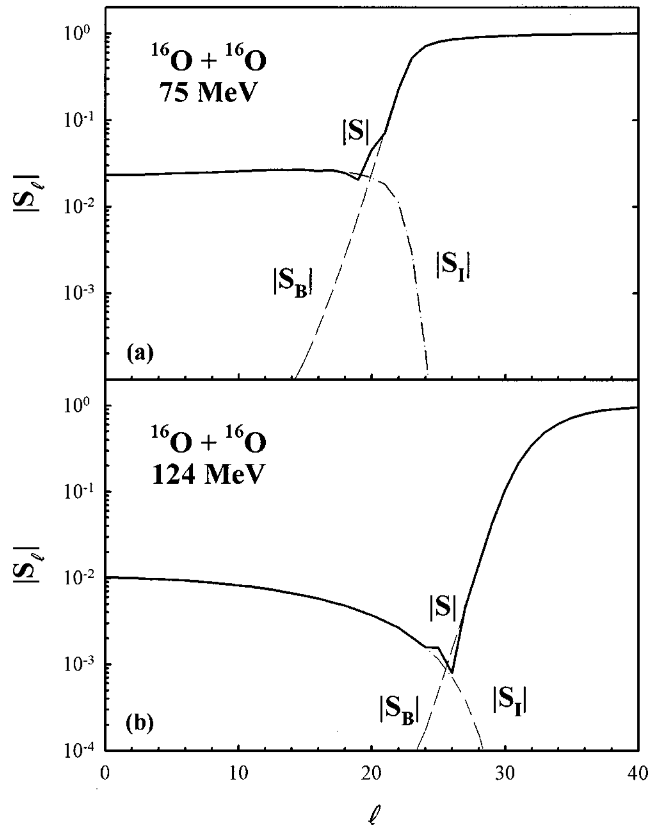

FIG. 8. Comparison of the barrier-wave and internal-wave components of the *S* matrix at 75 and 124 MeV incident energies.

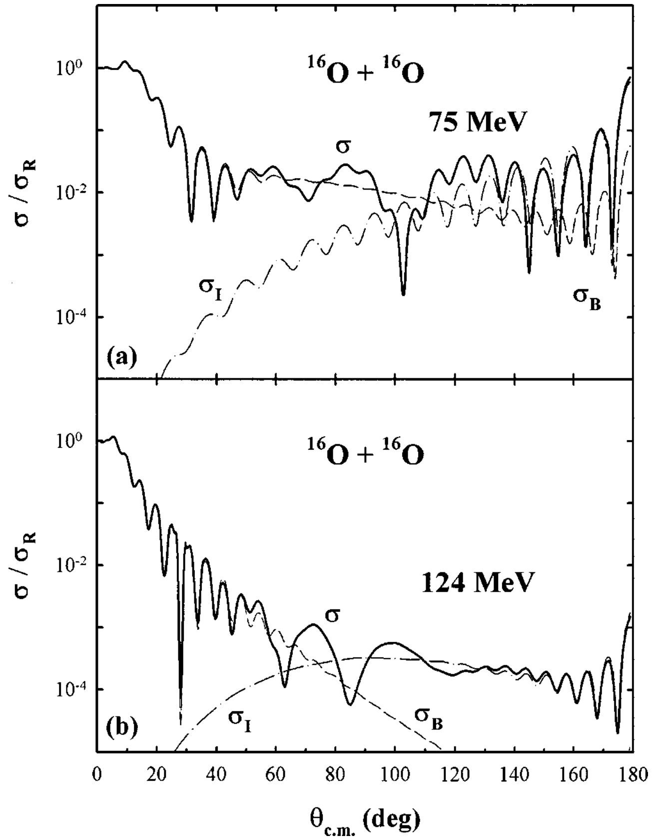

FIG. 9. Angular distributions corresponding to the barrier-wave and internal-wave components of the (unsymmetrized) $^{16}O+^{16}O$ optical model scattering amplitude at 75 and 124 MeV incident energies.

derived cross sections, as will be seen below (in this angular momentum region the barrier contribution supplied by the calculation is already more than three orders of magnitude smaller than $|S_I|$); the parameter W_2 will thus be fixed in the rest of this work to a value of 20 MeV.

In Fig. 8, we compare the B/I decompositions of the *S* matrix at 75 and 124 MeV; the 124 MeV results were obtained with the same parameters for the perturbing potential as at 75 MeV. One sees that the 124 MeV results are similar to those obtained at 75 MeV, the most noticeable evolution with energy being a decrease of the strength of the internal contribution, and a general shift towards larger angular momenta of the cutoff of the two components. The decrease of the internal contribution at the cutoff is also found to be much smoother at the highest energy.

The barrier and internal wave contributions $\sigma_B(\theta) = |f_B(\theta)|^2$ and $\sigma_I(\theta)=|f_I(\theta)|^2$ to the cross sections at 75 and 124 MeV, corresponding to these *S* matrix elements, are plotted in Fig. 9. Before we comment on the results, we like to point out that at 75 MeV, where semiclassical calculations could be carried out consistently, the agreement between the angular distributions obtained within the quantum-mechanical perturbative method and the semiclassical results is virtually perfect (even calculations carried out with $W_2 = 0$ produce results nearly indistinguishable from the semiclassical ones at the scale of Fig. 9). At 124 MeV our semiclassical code was unable to deliver numerically stable results, in contrast with the quantum-mechanical code which produces only marginal instabilities in the barrier contribution at extreme backward angles; we thus conclude that the quantum-mechanical perturbative method can be used reliably on the whole energy range we are investigating here.

The results of the B/I decomposition are qualitatively similar at the two energies—although the relative importance of the barrier and internal components at large angles is rather different at 75 and 124 MeV. In particular, the forward angle region, including the familiar Fraunhofer diffractive features, is seen to be dominated by the barrier contribution, while at large angles (more especially at 124 MeV), the internal contribution accounts for the full cross section. At intermediate angles, the broad structures observed in the full quantum cross section are seen to result from strong interference effects between the two subamplitudes, which turn out to have comparable magnitudes in this angular range.

In the B/I decomposition approach, the origin of the Airy minima and maxima seen in the full cross section thus stands out remarkably clearly: these are caused by an interplay between the waves which have been diffracted by the optical potential surface, and those which have survived the penetration of the nuclear interior. The presence of this second component, which can only subsist in a context of incomplete absorption, is a prerequisite to the appearance of Airy features in the angular distribution. Indeed repeating the calculation at 124 MeV with increasing values of the imaginary

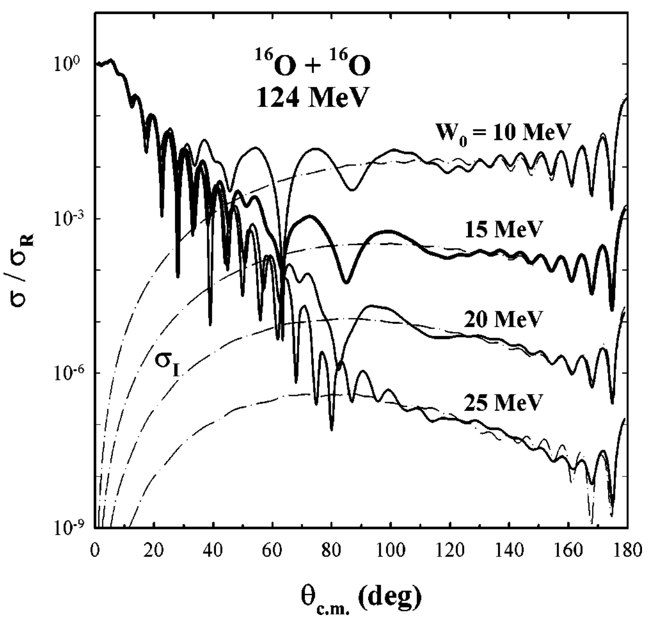

FIG. 10. Effects at 124 MeV on the full cross section (full lines) and on the internal-wave component (dot-dashed lines) of a decrease or of an increase of the imaginary potential strength (the nominal absorption at this energy is $W_0=15$ MeV).

potential strength makes the internal contribution smaller (less change is observed in the barrier contribution), and as a result the Airy oscillations vanish progressively and the full cross section becomes more and more diffractive (Fig. 10).

The present analysis thus amply confirms the remarkable transparency displayed by the ^{16}O+^{16}O system for $E/A < 10$ MeV, which is not unlike that found in some light ion systems such as $\alpha+{}^{16}$O or $\alpha+{}^{40}$Ca at low energy [23]. For these systems, symmetrization effects do not hide the behavior of the scattering amplitude at extreme backward angles; this is the region where the internal wave contribution is the largest and gives rise to the famous ALAS phenomenon.

It is interesting to inquire how the results discussed for the present system survive to symmetrization. In Fig. 11, we present the 124 MeV barrier-wave and internal-wave contributions to the *symmetrized* optical model cross section. In contrast with the N/F decomposition, where the farside contribution dominates the scattering in the important angular region around 90° and accounts by itself for the experimental data, the B/I decomposition shows clearly the angular region where the contribution of the nuclear interior is important (we note in addition that although symmetrized versions of the nearside and farside components of the scattering amplitude can be constructed, they present the unpleasant feature to contain contributions from both the even *and* odd partial waves, since the Legendre functions of the second kind do not obey the same symmetry rule as the ordinary Legendre polynomials for projectile-target exchange, and as a matter of fact they are never displayed).

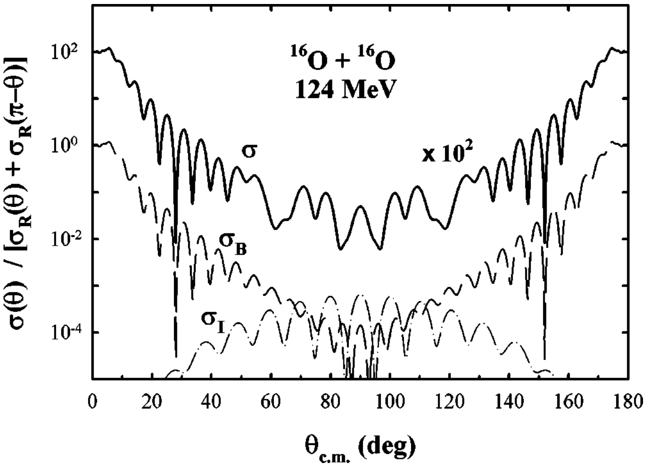

FIG. 11. Decomposition of the symmetrized optical model angular distribution at 124 MeV into its barrier-wave and internal-wave components.

At 124 MeV, the symmetrized internal contribution is seen (Fig. 11) to dominate the scattering from 70 to 110 °; the Airy minimum which was seen in the unsymmetrized cross section near 60° remains quite conspicuous in the symmetrized cross section (the symmetrized barrier and internal components have similar magnitudes in this angular region), while that near 90° has become less prominent. The oscillations seen in the symmetrized barrier and internal wave components around 90° are entirely due to symmetrization: indeed a look at Fig. 9(b) shows that, between 60 and 120 °, the unsymmetrized σ_B and σ_I behave smoothly with angle. Moreover the Airy minima around 60 (and 120) and 90 °, and more generally the complicated structure of the symmetrized angular distribution between 40 and 140 °, are seen to result from interferences between the more regularly oscillating barrier-wave and internal-wave amplitudes.

The barrier-wave/internal-wave decomposition of the scattering amplitude also helps to understand the role of the small surface absorption which has been used in recent works to improve the optical model description of the data [6,7]. For illustrative purposes we will concentrate here on the 115.9 MeV potential of Nicoli *et al.* [6], which includes a (seemingly modest) derivative Woods-Saxon imaginary potential, with $W_D=0.392$ MeV, $R_D=7.22$ fm, $a_D=0.20$ fm; the ability of this potential to reproduce the data is compared in Fig. 12(a) with that of the potential of Table I. One sees that the main effect of using a surface term is to improve the agreement in the region around 90°, where interference effects between the barrier and internal components are the strongest. The barrier-internal wave decomposition itself is carried out for the potential of Ref. [6] in Fig. 12(b), with (dashed line) and without (full line) the surface term. Whereas the introduction of the surface term modifies the internal contribution in a negligible way, one sees that the response of the barrier cross section is an *increase* at large angles, in an angular region where, in the absence of the surface term, it was very low.

The effect of the surface absorption introduced, which peaks outside of the barrier radius (cf. Fig. 3) and has a very small diffuseness, is thus to produce additional reflection, which complements that due to the potential barrier; in contrast the absorptive effects of this term are negligible, since the flux corresponding to the internal part, which has to cross this absorptive peak twice, is hardly affected. The result of

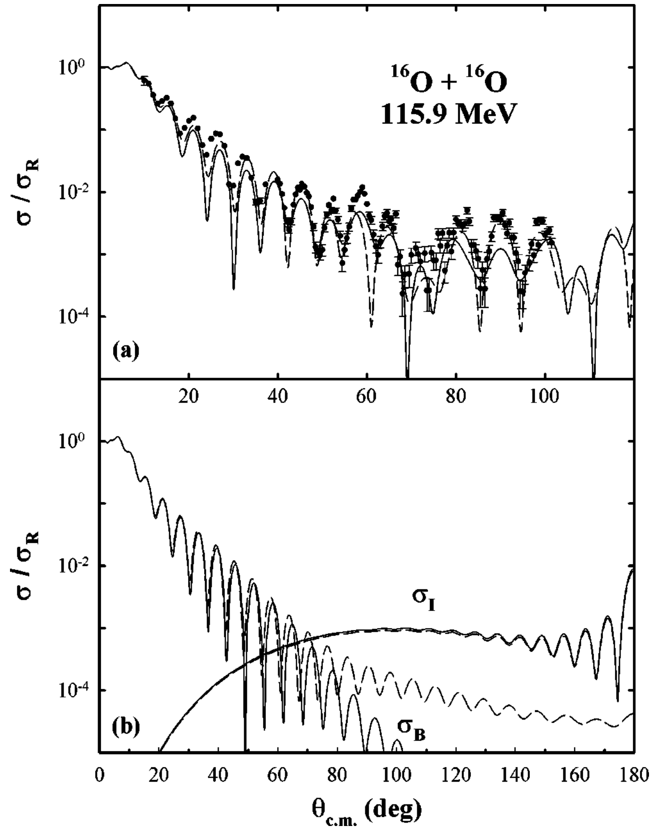

FIG. 12. (a) Optical model fits to the 115.9 MeV data including (dashed line) or excluding (full line) a surface imaginary term; (b) effect on the barrier-wave and internal-wave cross sections of the introduction of a sharply peaked surface imaginary term (see text; full line: without surface absorption, dashed line: inclusion of a sharply peaked surface absorption).

this increase of the barrier contribution is to perturb the interference effects between the barrier and internal components, and to offer more flexibility to reproduce the delicate pattern displayed by the data around 90° (remember that the scattering subamplitudes have still to be symmetrized). Because of this delicate interplay the energy dependence of the calculated cross sections also becomes more intricate. Whatever the phenomenological merits of these additional surface imaginary potentials, the physical origin of the extra reflection they produce is not clear and should be investigated in more detail.

In order to explain the origin of the gross structure observed in the farside angular distributions, obtained from the Fuller N/F decomposition, one has to postulate in a deflection function picture that two different ranges of angular momenta contribute to the farside amplitude; the cross sections $\sigma_{F,<}$ and $\sigma_{F,>}$ corresponding to these two ranges have sometimes been estimated in an approximate way by resorting to the so-called interpolated envelope technique (see Sec. II B). It turns out that application of this technique to the (unsymmetrized) optical model farside angular distributions of the present study involves some degree of arbitrariness: indeed because of the rather wide separation between the successive maxima and minima, the drawing of the envelope curves is far from being unique. In fact these two contributions can be obtained in a much more natural and rigorous way by performing a N/F decomposition of the barrier-wave and internal-wave amplitudes; this is an easy task since f_B and f_I are expressed in the form of partial wave series [Eqs. (10) and (11)]: one has simply to replace the Legendre polynomials $P_l(\cos\theta)$ by the angular functions $\tilde{Q}_l^{(\pm)}(\cos\theta)$ according to the prescription of Eq. (5). The calculation supplies four subamplitudes, which in a natural notation will be noted $f_{B,N}$, $f_{B,F}$, $f_{I,N}$, and $f_{I,F}$; their status is summarized in Fig. 13.

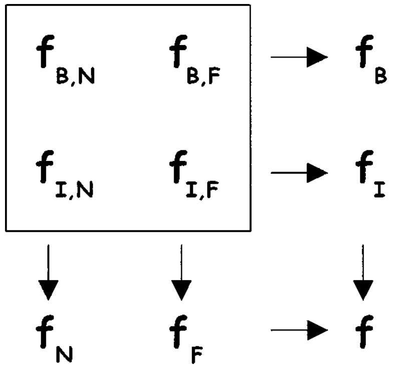

FIG. 13. The various subamplitudes into which the full elastic scattering amplitude is decomposed in the present work.

The result of the decomposition of the 124 MeV farside amplitude into its barrier and internal components is presented in Fig. 14. The strongly oscillating farside cross section, whose behavior accounts for the Airy structure of the full cross section, is seen to have been decomposed into two components, $\sigma_{B,F}$ and $\sigma_{I,F}$, which have all the properties of the cross sections $\sigma_{F,>}$ and $\sigma_{F,<}$ of the N/F approach. Indeed by construction these two components correspond to different ranges of angular momenta (inspection of Fig. 8 shows that the barrier and internal S matrix components are largely separated in angular momentum space), and in addi-

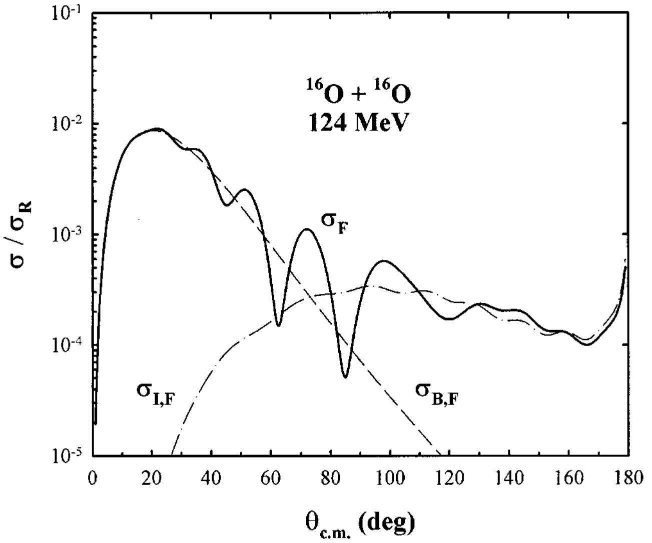

FIG. 14. Farside component, and farside contributions to the 124 MeV $^{16}O+^{16}O$ barrier-wave (dashed line) and internal-wave (dot-dashed line) components.

tion the corresponding cross sections now behave smoothly as a function of angle.

The main advantage of the B/I approach is that these two contributions to the cross section are much easier to compute than in a fully semiclassical context [39,27]; on the other hand, their calculation does no more rely on a qualitative construction like that involved in the interpolated envelope technique, and they are thus obtained in a more rigorous way. It is worth pointing out that a calculation of the nearside and farside components of the barrier and internal contributions to the ^{12}C+^{12}C elastic scattering amplitude at 51 MeV center of mass energy was presented by Rowley, Doubre, and Marty, in a pioneering paper [43] where the beat structure observed in the farside cross section was shown like here to be due to the interference of the farside contributions to the barrier and internal components; however the beat structure observed in the farside cross section was not associated at that time with an Airy mechanism, and even the physical significance of the deep potentials needed to produce these features was unclear. To the best of our knowledge, this type of decomposition was never attempted in later studies; in particular it is completely absent in the most recent compilation devoted to light heavy-ion scattering [1].

Though less instructive, the decomposition of the nearside amplitude into its barrier and internal components provides some interesting insight into the ^{16}O+^{16}O scattering mechanism. In particular, it supports the interpretation of Ref. [6] concerning the refractive origin of the oscillations seen in the full cross section beyond the diffractive Fraunhofer oscillations at low energy. In Fig. 15(b), we present the cross sections $\sigma_{B,N}$ and $\sigma_{I,N}$ corresponding to the barrier-wave and internal-wave components of the nearside amplitude at 75 MeV incident energy [Fig. 15(a) shows the farside contributions to the barrier-wave and internal-wave components at the same energy]. Whereas the barrier contribution dominates the nearside cross section—which at first decreases rapidly with angle—up to about 60°, the internal contribution becomes rapidly dominant beyond that angle and is responsible for the large value assumed there by the full nearside cross section, and thus for the oscillations seen in the full cross section beyond 80° (see Fig. 5); the refractive origin of these oscillations is thus obvious, since the internal contribution, which originates from close projectile-target encounters, is clearly associated with a refractive mechanism.

To understand better the mechanism producing the Airy maxima and minima in the farside cross section, we conclude this long section with a discussion on the evolution of the phases $\phi_{B,F}$ and $\phi_{I,F}$ of the barrier-wave and internal-wave farside amplitudes—these quantities are not supplied by the interpolated envelope technique—as a function of the scattering angle. In Fig. 16(a), we show these phases at 124 MeV as a function of the scattering angle, as well as their difference; the latter is plotted using an expanded scale in Fig. 16(b). These phases and their difference are seen to behave in a smooth way on most of the angular range. The positions of the Airy minima at 124 MeV, which correspond to the angles where the phase difference $\phi_{B,F}-\phi_{I,F}$ is an odd multiple of π, are identified in Fig. 16(b).

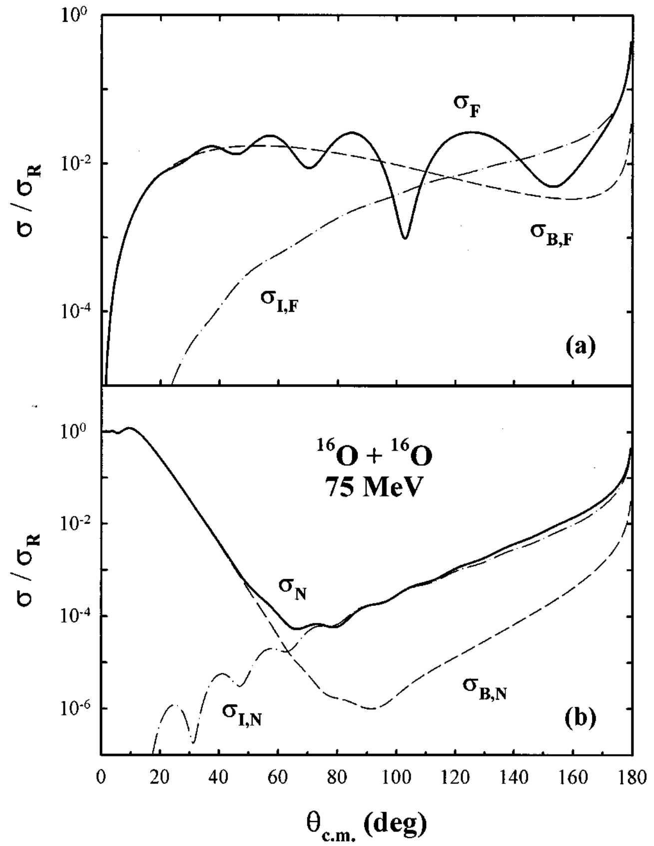

FIG. 15. (a) Farside and (b) nearside contributions to the barrier-wave (dashed line) and internal-wave (dot-dashed line) components of the 75 MeV ^{16}O+^{16}O optical model cross section.

Barrier-wave/internal-wave interference also underlies the presence in the 90° (unsymmetrized) excitation function of minima, corresponding to the crossing of the successive Airy minima, which shift to smaller angles as energy increases; this mechanism has been thoroughly investigated by McVoy and Brandan [12], who showed how it explains the so-called ''elephants'' appearing in the experimental ^{12}C+^{12}C excitation function at 90° between 70 and 130 MeV. In Fig. 17(b), we plotted the farside ^{16}O+^{16}O excitation function at 90° between 50 and 150 MeV, calculated using the parameters of the 124 MeV potential; the orders of the Airy minima responsible for the successive dips in the excitation function are identified in the figure. Of course because of the neglect of the energy dependence of the imaginary part of the potential, the absolute value of the cross section is under- (over-) estimated below (above) 124 MeV, but the location of the maxima and minima is not seriously affected by this assumption. Indeed, as can be seen in Fig. 10, the position of the Airy extrema is not sensitive to the exact absorption used (provided absorption does not become strong enough to eliminate the Airy structure); the energy of these minima agrees well with the measurements of Halbert *et al.* [44]. One sees again that the two contributing amplitudes $f_{B,F}$ and $f_{I,F}$ behave smoothly with energy; Fig. 17(a) displays the energy evolution of the phases of the barrier and internal contributions to the farside amplitude at 90° and their difference $\phi_{I,F}-\phi_{B,F}$, and identifies the energies of the Airy

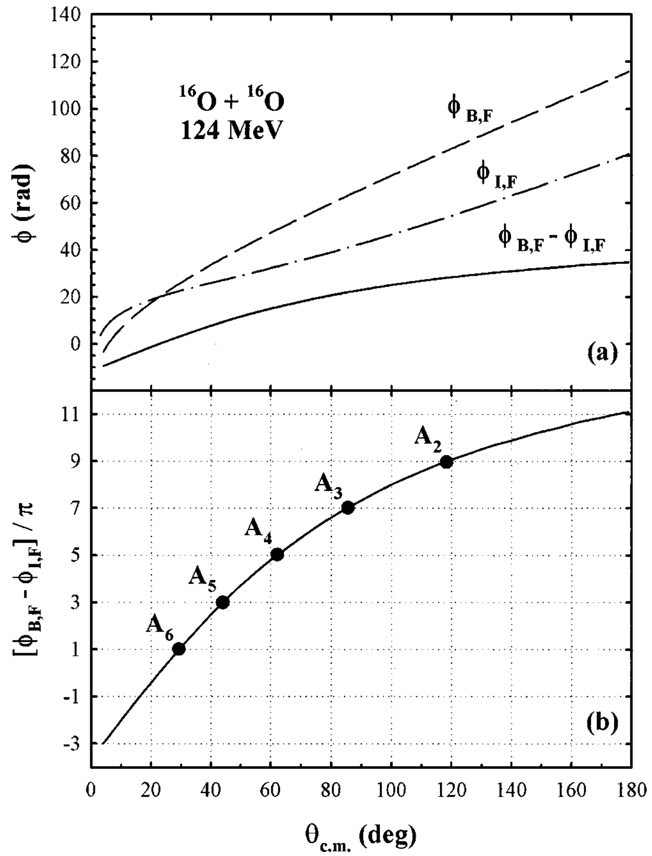

FIG. 16. (a) Evolution with angle of the phases $\phi_{B,F}$ and $\phi_{I,F}$ of the farside contributions to the barrier-wave (dashed line) and internal-wave (dot-dashed line) components of the $^{16}O+^{16}O$ elastic scattering amplitude at 124 MeV, and of their difference; (b) identification, on an enlarged view of $\phi_{B,F}-\phi_{I,F}$, of the Airy minima, which correspond to a destructive interference between the barrier-wave and internal-wave components.

minima where this phase difference is an odd multiple of π.

As a summary of the above discussion, we identify in Fig. 18 the origin of the various structures seen in the symmetrized cross section at 124 MeV; the thin full and dashed lines are the unsymmetrized cross section $\sigma(\theta)$ and its ''mirror image'' $\sigma(\pi-\theta)$. In addition to the Fraunhofer oscillations—due to nearside/farside interference—and to the third (A_3) and fourth (A_4) Airy minima—due to barrier-wave/internal-wave interference—one observes, in the region of the Airy maximum separating A_3 and A_4, oscillations due to symmetrization interference. This plot recalls how delicate and complex interference effects can become in transparent systems, and it explains why a precise description of the experimental excitation functions and angular distributions for these systems will for a long time remain such a formidable challenge.

2. Evolution with energy

In the previous subsection we have presented results obtained from the N/F and B/I decomposition techniques at selected energies; in the present one we gather the results of calculations performed at all the available energies between 75 and 145 MeV, in order to get an overall picture of the general evolution of the various contributions to the $^{16}O+^{16}O$ elastic scattering cross sections.

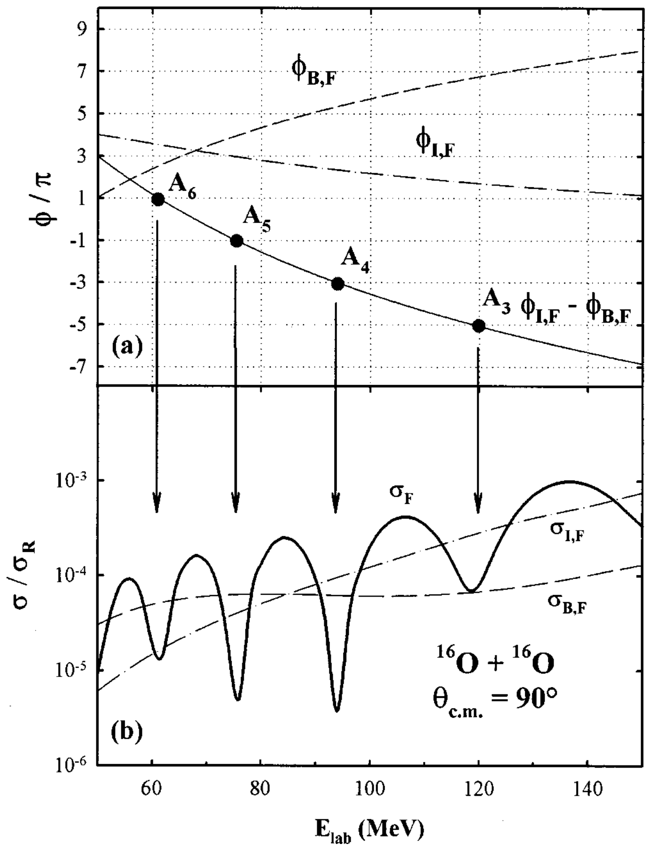

FIG. 17. (a) Evolution with energy of the phases $\phi_{I,F}$ and $\phi_{B,F}$ of the farside contributions to the barrier-wave (dashed line) and internal-wave (dot-dashed line) components of the $^{16}O+^{16}O$ elastic scattering amplitude at 90°, and of their difference; the successive Airy minima corresponding to a destructive interference between these components are also identified; (b) evolution with energy of the farside component, and of the farside contributions to the barrier-wave and internal-wave components at 90°. All the calculations were performed using the parameters of the 124 MeV optical model potential.

We first display in Fig. 19 the barrier-wave and internal-wave contributions to the full unsymmetrized quantum cross section (in this and similar figures, curves are shifted by a factor of 10 when going from one energy to the next). The most striking feature of these angular distributions is their regular evolution with incident energy, which departs from the much more irregular behavior of the full cross section. Beyond the Fraunhofer oscillations, which as expected shift to smaller angles with increasing energy, the barrier-wave cross section is seen to decrease with angle, at a rate which increases smoothly with incident energy. A striking exception to this regular behavior is observed at 92 MeV, and to some degree at 95 MeV, where both the slope and oscillatory behavior of the cross sections contrast with those observed at neighboring energies. A look at Fig. 1 shows that the potential of Nicoli [26] is rather unsuccessful at 92 and 95 MeV, and inspection of Table I reveals a sharp decrease of the

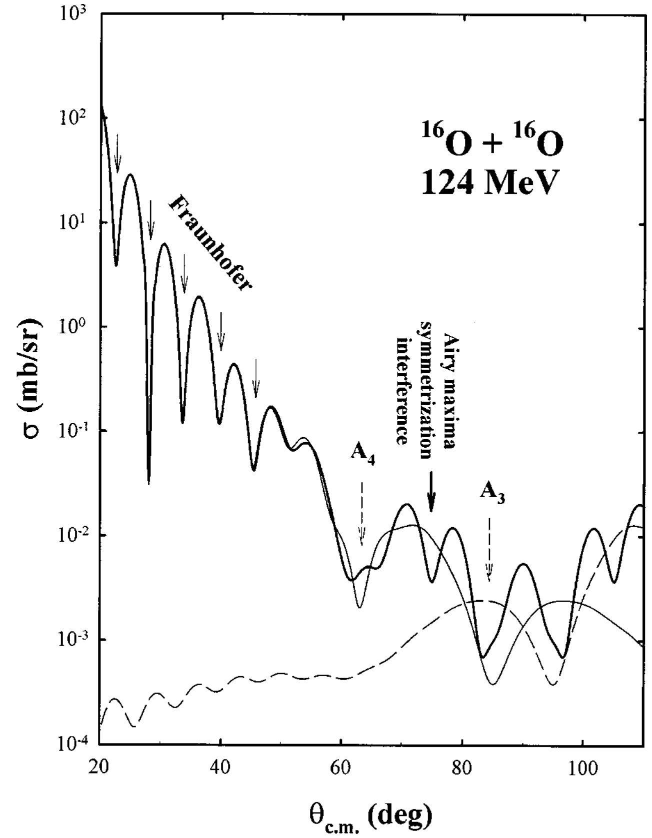

FIG. 18. Interpretation of the minima appearing in the ^{16}O + ^{16}O optical model symmetrized angular distribution at 124 MeV (thick full line); the thin full and dotted lines represent the unsymmetrized cross section $\sigma(\theta)$ and its "mirror image" $\sigma(\pi-\theta)$, respectively.

imaginary diffuseness a_I between 87.2 and 92.4 MeV; the introduction of an additional surface imaginary potential in Ref. [6] does not improve significantly the situation at 92.4 MeV. On the other hand, the evolution of the internal-wave contribution is seen to be quite smooth, the main trend being a progressive disappearance of the oscillations at midangles and a gradual decrease of the slope at mid and large angles. A careful look at Fig. 19 shows that despite its progressive decrease, the influence of the internal-wave contribution on the scattering becomes paradoxically more and more conspicuous with increasing energy, as a result of the faster decrease with angle of the slope of the barrier-wave cross section; this trend is already apparent in Fig. 9 where the respective role of the two components is compared at 75 and 124 MeV.

The evolution with energy of the full farside cross section is displayed in Fig. 20; this figure is similar to that provided by Nicoli *et al.* [6] for their folding model calculations (note that in the latter, the imaginary potential strength was reduced to half its normal value in order to emphasize the refractive effects). The change with energy of the location of the various Airy minima can be followed fairly easily in this plot; the crossing of the A_5, A_4, and A_3 minima at 90° is responsible for the minima seen in the corresponding excitation function around 75, 90, and 120 MeV (see Fig. 17). A careful look at the figure shows again that the 92 MeV far side angular distribution is not in line with those at neighboring energies.

The result of the decomposition of the farside amplitude into its barrier and internal components between 75 and 145 MeV is presented in Fig. 21. Comments about the anomalous behavior of the barrier contribution to the farside amplitude at 92 and 95 MeV can be repeated here. Once more the

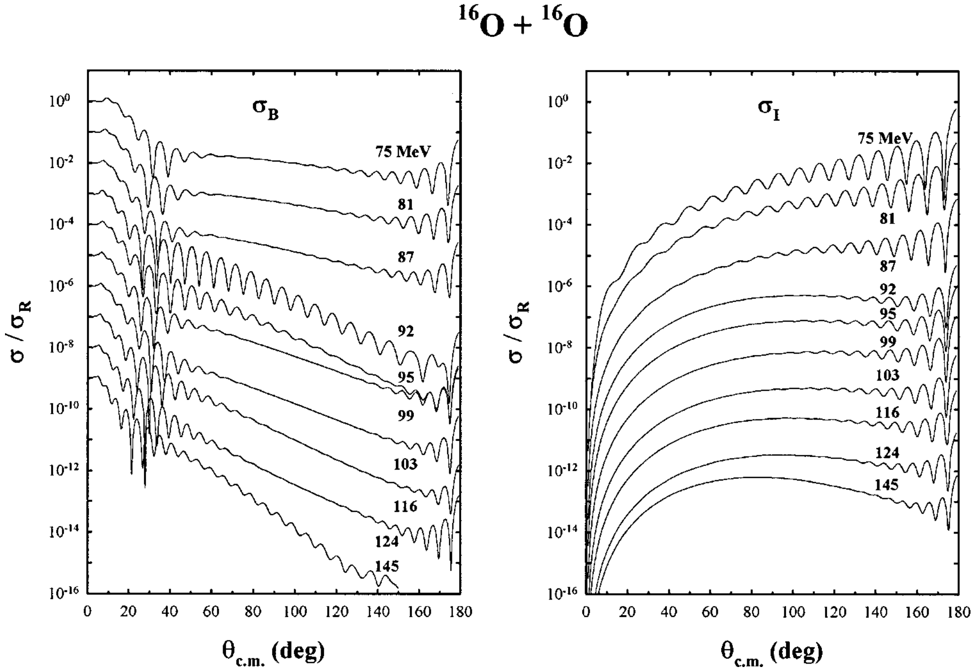

FIG. 19. Evolution between 75 and 145 MeV of the cross sections corresponding to the barrier-wave (left) and internal-wave (right) components of the ^{16}O+^{16}O optical model scattering amplitude.

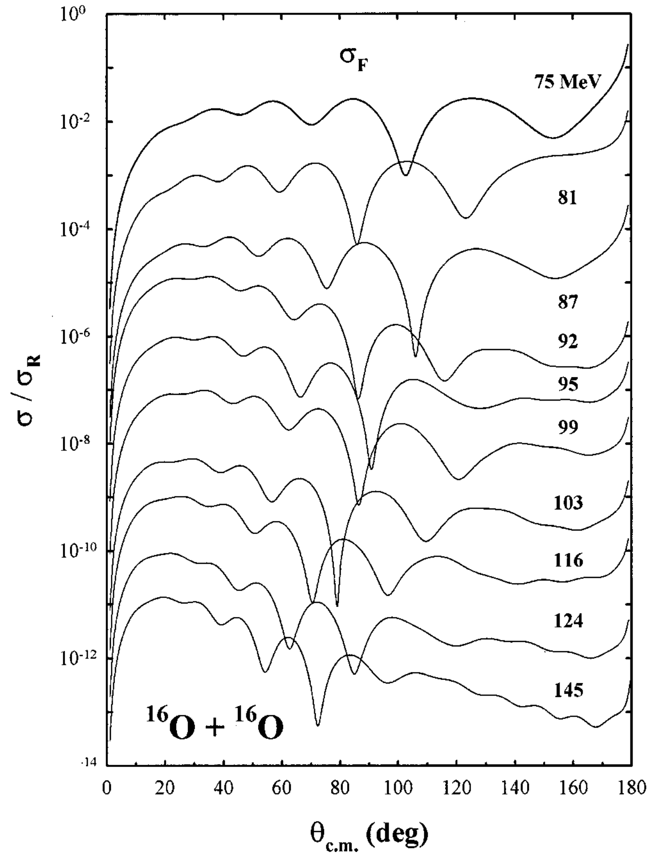

FIG. 20. Evolution between 75 and 145 MeV of the farside contribution to the optical model $^{16}O+^{16}O$ cross section.

oscillating—albeit reasonably regular—behavior of the farside cross section is seen to be explained in terms of two subamplitudes varying smoothly as a function of angle and energy. It is worth stressing again that the uncertainties involved for the present system in the drawing of the envelope curves needed for applying the interpolated envelope technique would have resulted in a less regular behavior of the two subamplitudes; because it would have been tedious to perform this qualitative decomposition for the ten energies considered in the present paper this construction was not attempted.

Finally we plot in Fig. 22 the modulus of the barrier and internal contributions to the optical model *S* matrix at six of the studied energies. The most conspicuous trend of the barrier contribution is a regular shift towards larger *l*-values as energy increases, a behavior expected for the *S* matrix in any strong absorption model. On the other hand, the internal *S* matrix profile also tends to shift to large *l* with increasing energy; its absolute value at low *l*, though decreasing with energy, is fairly stable since it remains of the order of one to two percents. It is the persistence of this seemingly modest contribution which is responsible for the distinctive refractive behavior observed in $^{16}O+^{16}O$ elastic scattering on the energy range studied here.

III. OTHER SYSTEMS

The two systems which come naturally to mind for a possible interpretation of Airy structure within the frame of the present approach are $^{12}C+^{12}C$ and $^{16}O+^{12}C$, which display indisputable refractive features. The $^{12}C+^{12}C$ system will be investigated in a forthcoming publication. We briefly report here the result of the decomposition of the elastic $^{16}O+^{12}C$ optical model cross section, at the selected incident energy of 132 MeV, into its various components, using one of the optical potentials recently proposed by Ogloblin *et al.* [5] (this potential has Woods-Saxon real and imaginary form factors and is noted WS1 in Ref. [5]). Here symmetrization effects do not hide the large angle behavior of the data, and two Airy minima are clearly observed around 60 and 80 °. The scattering is seen to be dominated by the internal-wave contribution at angles as small as 80° [Fig. 23(a)], which points to a transparency similar to that found in $^{16}O+^{16}O$ scattering. The most prominent Airy minimum, located at 80° (it turns out to be A_2 [5]), which is the result of the interference between the barrier-wave and internal-wave components, is particularly sharp because these two components happen to have similar magnitudes in this angular region. The decomposition of the farside contribution, which carries the Airy

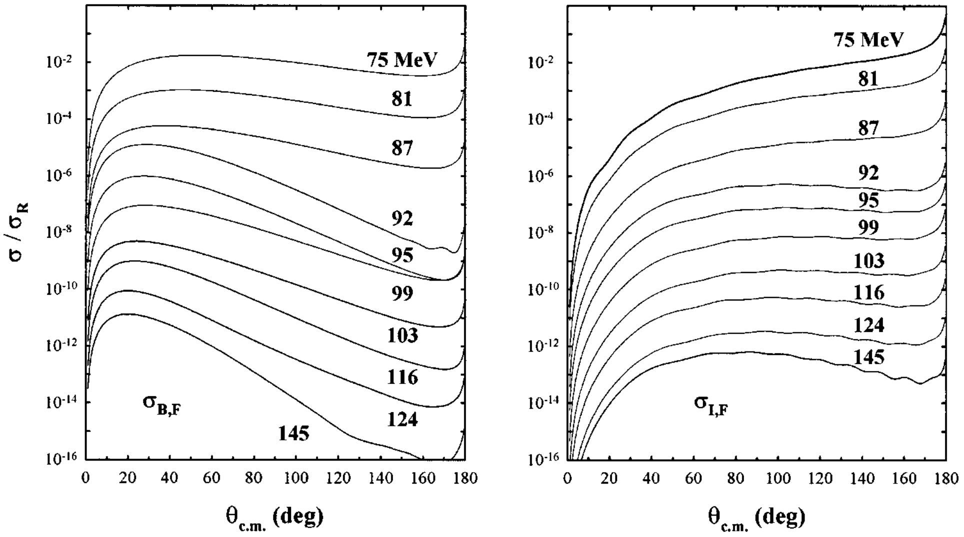

FIG. 21. Evolution between 75 and 145 MeV of the cross sections corresponding to the farside contributions to the barrier-wave (left) and internal-wave (right) components of the $^{16}O+^{16}O$ optical model scattering amplitude.

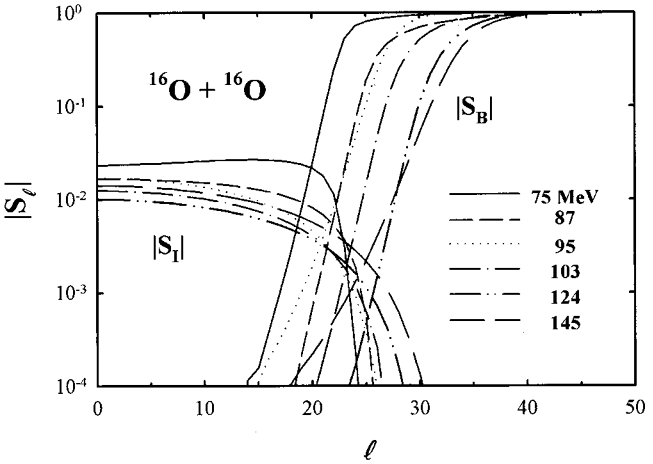

FIG. 22. Barrier-wave and internal-wave components of the $^{16}O+^{16}O$ optical model elastic scattering *S* matrix at 75, 87, 95, 103, 124, and 145 MeV incident energies.

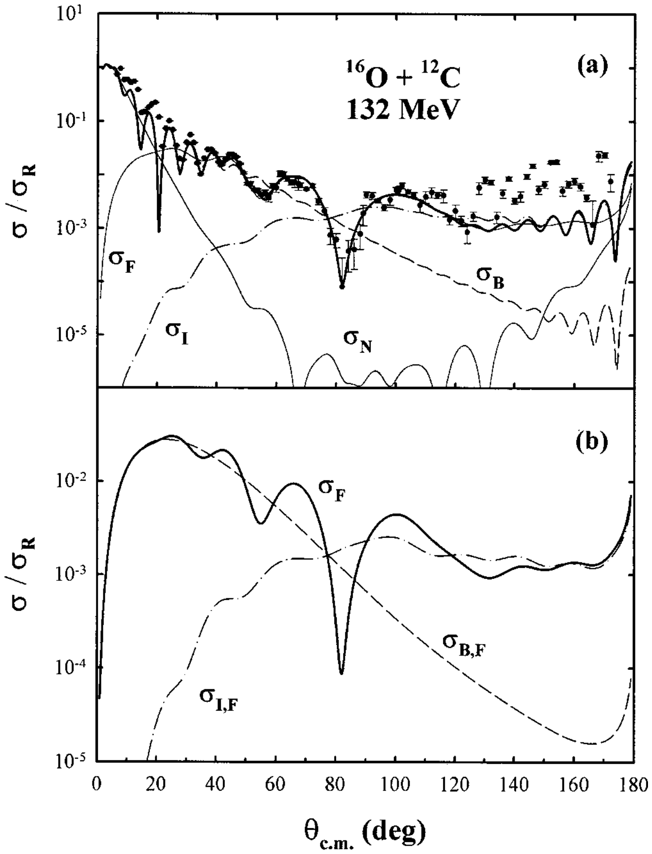

FIG. 23. (a) N/F (thin lines) and B/I components (thin dashed/dot-dashed lines) of the $^{16}O+^{12}C$ optical model cross section (thick full line) which fits the data (filled circles) at 132 MeV incident energy; (b) farside component, and farside contributions to the barrier-wave (dashed line) and internal-wave (dot-dashed) components of the cross section. The calculations were carried out with the optical model parameters of Ogloblin *et al.* [5].

minima, into its barrier-wave and internal-wave components, appears in Fig. 23(b).

Like in light-ion scattering, the remarkable transparency displayed by the $^{16}O+^{16}O$ and $^{16}O+^{12}C$ systems is an exceptional feature which is lost in most neighboring systems. As a counter-example to the cases studied above, we show here the result of a B/I decomposition of the $^{18}O+^{12}C$ elastic scattering amplitude at 100 MeV incident energy (Fig. 24). The potential used, supplied by Szilner *et al.* [45], fits reasonably well the experimental data, which first appeared in Ref. [26]; it has Woods-Saxon squared real and imaginary geometries and includes a surface absorptive term. In the notations of Eqs. (2)–(4), its parameters are $U_0=288$ MeV, $R_R=4.08$ fm, $a_R=0.69$ fm, $W_0=20.97$ MeV, $R_I=4.744$ fm, $a_I=0.065$ fm, $W_D=9.3$ MeV, $R_D=5.80$ fm, and $a_D=0.59$ fm (note again the exceedingly small volume absorption diffuseness). A good fit to the $^{16}O+^{12}C$ angular distribution at the same energy is obtained with similar parameters, but with a weaker surface absorptive term [26]. The main difference between the two angular distributions is that the Airy minimum seen in $^{16}O+^{12}C$ around 80 ° has completely vanished in the $^{18}O+^{12}C$ angular distribution. The result of the decomposition of the elastic scattering amplitude for the latter system explains the disappearance of this feature in $^{18}O+^{12}C$: indeed, because of the stronger absorption needed in this case, the internal-wave cross section is now about three orders of magnitude lower than in the $^{16}O+^{12}C$ case, and its contribution to the scattering has become negligibly small.

IV. CONCLUSIONS

In this paper, we have systematically applied the barrier-wave/internal-wave decomposition technique, first introduced in a semiclassical context by Brink and Takigawa, to the $^{16}O+^{16}O$ elastic scattering optical model angular distributions of Nicoli [26] and of Khoa *et al.* [7] between 75 and 145 MeV, an energy region where strong refractive effects—in particular Airy maxima and minima—are clearly observed. The barrier-wave contribution to the elastic scattering amplitude corresponds to the part of the incident flux which is reflected at the barrier of the effective potential, while the internal-wave contribution is due to the part of the flux which crosses the barrier and reemerges in the elastic channel after reflection at the most internal turning point. Despite of its success in elucidating the mechanism of light-ion scattering in an incomplete absorption context, and of the existence of a few pioneering papers drawing the attention on its potentialities, this type of decomposition has up to now practically never been used for analyzing light heavy-ion scattering results.

Instead of performing this decomposition within a semiclassical frame, which requires rather complex programming, use was made here of a fully quantum-mechanical approach which can be implemented using any standard optical model code. This method relies on the study of the response of the elastic scattering *S* matrix to small modifications of the optical model potential.

In this approach, the $^{16}O+^{16}O$ Airy minima are found to be due to the interference of the barrier-wave and internal-wave subamplitudes. This result contrasts with the picture supplied by the often-used nearside/farside decomposition

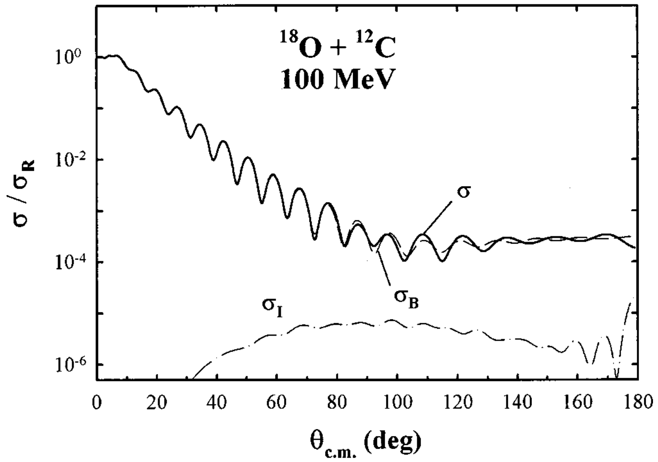

FIG. 24. Barrier-wave/internal-wave decomposition (thin dashed/dot-dashed lines) for $^{18}\mathrm{O}+^{12}\mathrm{C}$ elastic scattering at 100 MeV, using the potential of Szilner *et al.* [45].

technique, in which the Airy minima are fully carried by the farside contribution, and which does thus not supply by itself an explanation for the occurrence of this structure. The existence of a substantial internal-wave contribution to the scat tering provides the most direct evidence for the exceptional transparency displayed by the $^{16}\mathrm{O}+^{16}\mathrm{O}$ system.

By combining the barrier-wave/internal-wave and nearside/farside decomposition techniques, it is possible to calculate in a straightforward way the two components—in fact the farside contributions to the barrier-wave and internal-wave components—underlying the Airy oscillations of the farside component, which up to now could only be obtained through delicate semiclassical calculations or the use of an approximate empirical method.

A detailed examination of the results of the B/I decomposition between 75 and 145 MeV shows that, with the exception of the 92 and 95 MeV angular distributions, the barrier-wave and internal-wave components of Nicoli's optical model $^{16}\mathrm{O}+^{16}\mathrm{O}$ elastic scattering amplitude behave smoothly as a function of energy, as is also the case for the farside contributions to these subamplitudes. This contrasts with the behavior of the full cross section, where the effects of symmetrization superpose on barrier-wave/internal-wave and nearside/farside interference, which eventually leads to the very intricate energy dependence displayed by the experimental data.

We have applied the same decomposition techniques to two nonsymmetric systems, $^{16}\mathrm{O}+^{12}\mathrm{C}$ and $^{18}\mathrm{O}+^{12}\mathrm{C}$, at 132 MeV and 100 MeV incident energies, respectively. In the first case, Airy minima similar to those seen in $^{16}\mathrm{O}+^{16}\mathrm{O}$ elastic scattering are observed—and indeed the barrier-wave/internal-wave decomposition reveals the existence of a sizeable internal component—while in the second case none is visible as a result of a stronger absorption, which makes the internal-wave contribution to the cross section about three orders of magnitude smaller.

In conclusion, we hope to have demonstrated that the barrier-wave/internal-wave decomposition technique, which complements nicely the nearside/farside approach, brings useful information on the mechanism of light heavy-ion elastic scattering, and that it deserves to be used in a more systematic way in that field.

ACKNOWLEDGMENTS

We would like to express our sincere thanks to Professor Fl. Haas and Professor C. Beck for supplying the $^{16}\mathrm{O}+^{16}\mathrm{O}$ Strasbourg elastic scattering data and a copy of Dr. M.-P. Nicoli's thesis, and Professor A. A. Ogloblin and Professor A. S. Dem'yanova for providing their recent $^{16}\mathrm{O}+^{12}\mathrm{C}$ experimental data. One of the authors (S.O.) thanks Professor W. von Oertzen, Professor H. G. Bohlen, and Professor Z. Basrak for useful discussions. S.O. has been supported by a Grant-in-aid for Scientific Research of the Japan Society for Promotion of Science (No. 12640288).

---

[1] M. E. Brandan and G. R. Satchler, Phys. Rep. **285**, 143 (1997), and references therein.
[2] R. G. Stokstad, R. M. Wieland, G. R. Satchler, C. B. Fulmer, D. C. Hensley, S. Raman, L. D. Rickertsen, A. H. Snell, and P. H. Stelson, Phys. Rev. C **20**, 655 (1979).
[3] A. A. Ogloblin, Dao T. Khoa, Y. Kondō, Yu. A. Glukhov, A. S. Dem'yanova, M. V. Rozhkov, G. R. Satchler, and S. A. Goncharov, Phys. Rev. C **57**, 1797 (1998).
[4] M. P. Nicoli, F. Haas, R. M. Freeman, S. Szilner, Z. Basrak, A. Morsad, G. R. Satchler, and M. E. Brandan, Phys. Rev. C **61**, 034609 (2000).
[5] A. A. Ogloblin, Yu. A. Glukhov, W. H. Trzaska, A. S. Dem'yanova, S. A. Goncharov, R. Julin, S. V. Klebnikov, M. Mutterer, M. V. Rozhkov, V. P. Rudakov, G. P. Tiorin, Dao T. Khoa, and G. R. Satchler, Phys. Rev. C **62**, 044601 (2000).
[6] M. P. Nicoli, F. Haas, R. M. Freeman, N. Aissaoui, C. Beck, A. Elanique, R. Nouicer, A. Morsad, S. Szilner, Z. Basrak, M. E. Brandan, and G. R. Satchler, Phys. Rev. C **60**, 064608 (1999).
[7] Dao T. Khoa, W. von Oertzen, H. G. Bohlen, and F. Nuoffer, Nucl. Phys. **A672**, 387 (2000).
[8] M. E. Brandan, M. Rodríguez-Villafuerte, and A. Ayala, Phys. Rev. C **41**, 1520 (1990).
[9] M. S. Hussein and K. W. McVoy, Prog. Part. Nucl. Phys. **12**, 103 (1984).
[10] K. W. McVoy and G. R. Satchler, Nucl. Phys. **A417**, 157 (1984).
[11] M. E. Brandan, S. H. Fricke, and K. W. McVoy, Phys. Rev. C **38**, 673 (1988).
[12] K. W. McVoy and M. E. Brandan, Nucl. Phys. **A542**, 295 (1992).
[13] M. E. Brandan, M. S. Hussein, K. W. McVoy, and G. R. Satchler, Comments Nucl. Part. Phys. **22**, 77 (1996).
[14] R. C. Fuller, Phys. Rev. C **12**, 1561 (1975).
[15] R. G. Newton, *Scattering Theory of Waves and Particles* (Springer-Verlag, New York, 1982).
[16] J. Knoll and R. Schaeffer, Ann. Phys. (N.Y.) **97**, 307 (1976).

[17] K. W. McVoy, H. M. Khalil, M. M. Shalaby, and G. R. Satchler, Nucl. Phys. **A455**, 118 (1986).
[18] Dao T. Khoa, G. R. Satchler, and W. von Oertzen, Phys. Rev. C **56**, 954 (1997).
[19] D. M. Brink and N. Takigawa, Nucl. Phys. **A279**, 159 (1977).
[20] F. Michel, J. Albiński, P. Belery, Th. Delbar, Gh. Grégoire, B. Tasiaux, and G. Reidemeister, Phys. Rev. C **28**, 1904 (1983).
[21] D. M. Brink, *Semi-classical Methods for Nucleus-Nucleus Scattering* (Cambridge University Press, Cambridge, England, 1985).
[22] F. Brau, F. Michel, and G. Reidemeister, Phys. Rev. C **57**, 1386 (1998).
[23] F. Michel, S. Ohkubo, and G. Reidemeister, Prog. Theor. Phys. Suppl. **132**, 7 (1998), and references therein.
[24] J. Albiński and F. Michel, Phys. Rev. C **25**, 213 (1982).
[25] F. Michel, F. Brau, G. Reidemeister, and S. Ohkubo, Phys. Rev. Lett. **85**, 1823 (2000).
[26] M. P. Nicoli, thesis, Strasbourg, 1998 (Int. Rep. IReS 98-16).
[27] E. Stiliaris, H. G. Bohlen, P. Fröbrich, B. Gebauer, D. Kolbert, W. von Oertzen, M. Wilpert, and Th. Wilpert, Phys. Lett. B **223**, 291 (1989).
[28] H. G. Bohlen, E. Stiliaris, B. Gebauer, W. von Oertzen, M. Wilpert, Th. Wilpert, A. Ostrowski, Dao T. Khoa, A. S. Demyanova, and A. A. Ogloblin, Z. Phys. A **346**, 189 (1993).
[29] G. Barnitzky, A. Blazevic, H. G. Bohlen, J. M. Casandjian, M. Chartier, H. Clement, B. Gebauer, A. Gillibert, Th. Kirchner, Dao T. Khoa, A. Lepine-Szily, W. Mittig, W. von Oertzen, A. N. Ostrowski, P. Roussel-Chomaz, J. Sigler, M. Wilpert, and Th. Wilpert, Phys. Lett. B **365**, 23 (1996).
[30] Y. Sugiyama, Y. Tomita, H. Ikezoe, Y. Yamanouchi, K. Ideno, S. Hamada, T. Sugimitsu, M. Hijiya, and Y. Kondō, Phys. Lett. B **312**, 35 (1993).
[31] Y. Kondō, Y. Sugiyama, Y. Tomita, Y. Yamanouchi, H. Ikezoe, K. Ideno, S. Hamada, T. Sugimitsu, M. Hijiya, and H. Fujita, Phys. Lett. B **365**, 17 (1996).
[32] Y. Kondō, F. Michel, and G. Reidemeister, Phys. Lett. B **242**, 340 (1990).
[33] M. E. Brandan and G. R. Satchler, Phys. Lett. B **256**, 311 (1991).
[34] D. T. Khoa, W. von Oertzen, A. Faessler, M. Ermer, H. Clement, and W. von Oertzen, Phys. Lett. B **260**, 278 (1991).
[35] R. Greenler, *Rainbows, Halos, and Glories* (Cambridge University Press, Cambridge, England, 1980).
[36] M. G. J. Minnaert, *Light and Colour in the Outdoors* (Springer-Verlag, New York, 1993).
[37] W. von Oertzen, Dao T. Khoa, and H. G. Bohlen, Europhys. News **31/2**, 5 (2000).
[38] H. G. Bohlen, X. S. Chen, J. G. Cramer, P. Fröbrich, B. Gebauer, H. Lettau, A. Miczaika, W. von Oertzen, R. Ulrich, and T. Wilpert, Z. Phys. A **322**, 241 (1985).
[39] S. H. Fricke, M. E. Brandan, and K. W. McVoy, Phys. Rev. C **38**, 682 (1988).
[40] R. da Silveira and Ch. Leclercq-Willain, Z. Phys. A **314**, 63 (1983).
[41] H. M. Khalil, K. W. McVoy, and M. M. Shalaby, Nucl. Phys. **A455**, 100 (1986).
[42] S. Y. Lee and N. Takigawa, Nucl. Phys. **A308**, 189 (1978).
[43] N. Rowley, H. Doubre, and C. Marty, Phys. Lett. **69B**, 147 (1977).
[44] M. L. Halbert, C. B. Fulmer, S. Raman, M. J. Saltmarsh, A. H. Snell, and P. H. Stelson, Phys. Lett. **51B**, 341 (1974).
[45] S. Szilner, M. P. Nicoli, Z. Basrak, R. M. Freeman, F. Haas, and A. Morsad, in *Proceedings of the 7th International Conference on Clustering Aspects of Nuclear Structure and Dynamics*, Rab, Croatia, 1999, edited by Z. Basrak, R. Čaplar, and M. Korolija (World Scientific, Singapore, 2000).